A Galerkin formulation for the nonlinear analysis of a flexible beam in channel flow

Filipe Soares, Jose Antunes, Vincent Debut, Christophe Vergez, Bruno Cochelin, Fabrice Silva

Journal of Fluids and Structures 118 (2023) 103842

Contents lists available at ScienceDirect

Journal of Fluids and Structures

journal homepage: www.elsevier.com/locate/jfs

A Galerkin formulation for the nonlinear analysis of a flexible beam in channel flow

Filipe Soares [a,*], Jose Antunes [a], Vincent Debut [a,b], Christophe Vergez [c], Bruno Cochelin [c], Fabrice Silva [c]

[a] Instituto Superior Técnico – Centro de Ciências e Tecnologias Nucleares, Lisboa, Portugal
[b] Instituto Politécnico de Castelo Branco – Escola de Artes Aplicadas, Castelo Branco, Portugal
[c] Aix-Marseille Université, CRNS, Centrale Marseille, LMA UMR7031, Marseille, France

ARTICLE INFO

Article history:
Received 26 October 2022
Received in revised form 12 January 2023
Accepted 1 February 2023
Available online 21 February 2023

Keywords:
Flow-induced vibration
Plate in axial flow
Reduced-order modeling
Spectral methods
Nonlinear dynamics

ABSTRACT

In this paper we propose a Galerkin formulation for the 1-D model describing the nonlinear flow-structure interaction of a flexible beam in confined flow. In broad terms, the system of PDEs is converted into a set of time-dependent equations (ODEs and algebraic) by developing all variables in terms of series of space-dependent orthogonal functions. The beam motion is developed in terms of its mode shapes while the flow pressure and velocity fields in each channel are developed in terms of Chebyshev polynomials. Additionally, a tau-variant of the Galerkin approach enables the enforcement of the nonlinear time-dependent boundary conditions in a well-posed manner. Ultimately, the resulting system is a set of nonlinear differential–algebraic equations that can be truncated at any suitable numbers of terms, leading to exploitable reduced formulations. Compared to CFD methods, this type of formulations is not only more computationally efficient, but also provide an easy discernment of the relevant parameters and often a more intuitive interpretation of results. Convergence studies, in terms of both the truncation of Chebyshev polynomials and beam modes, are performed to access to what extent reduced formulations are viable in different scenarios, including linear stability analysis as well as the calculation of limit-cycle oscillations with or without intermittent impacts between the beam and the side-walls. The presented framework can serve as a basis for a comprehensive analysis of the nonlinear dynamics of flexible beams in confined flow. Namely, it is well adapted to the use of bifurcation analysis tools for the continuation of periodic solutions, which will contribute to a richer understanding of the underlying physics occurring in this type of FSI systems. Moreover, the generic methodology presented here can also be adapted to different systems in the field of fluid–structure interaction, providing compact time-dependent formulations for nonlinear analysis.

1. Introduction

The dynamics of a flexible plate immersed in uniform axial flow are a widely studied subject and represent a canonical example of flow-induced vibration (Paidoussis, 2004; Nagakura et al., 2014). Systems of this type present a wide variety

* Corresponding author.
E-mail addresses: filipe.soares@ctn.tecnico.ulisboa.pt (F. Soares), jantunes@ctn.tecnico.ulisboa.pt (J. Antunes), vincentdebut@ipcb.pt (V. Debut), vergez@lma.cnrs-mrs.fr (C. Vergez), bruno.cochelin@centrale-marseille.fr (B. Cochelin), silva@lma.cnrs-mrs.fr (F. Silva).

https://doi.org/10.1016/j.jfluidstructs.2023.103842

of dynamical behavior and some aspects of their physical modeling remain a challenging task to this day. Moreover, because similar systems can be found in a large number of practical applications (e.g. paper industry, energy harvesting, wind musical instruments, palatal snoring etc.), it has motivated a large body of literature, dealing with various plate-flow configurations and using diverse modeling approaches (Alben, 2015; Hidalgo et al., 2015; Aurégan and Depollier, 1995; Avanzini and Walstijn, 2004).

One of the most important features defining the dynamics of plates subject to axial flow are the plate boundary conditions, for which Guo & Paidoussis have presented an elucidative study (Guo and Paidoussis, 2000). Assuming inviscid and incompressible flow, and using the linearized unsteady Bernoulli equation, they studied the relation between various plate boundary conditions and the type of instabilities emerging. Their analysis shows that plates can lose stability by divergence, single-mode flutter or coupled-mode flutter, depending on the support conditions at the leading and trailing edges. On the one hand, plates fixed at both ends (pinned or clamped) first lose stability by divergence, although post-divergent flutter may also occur. On the other hand, plates with at least one free-end undergo a flutter instability, either by single-mode or coupled-mode flutter depending on particular flow-plate configurations.

The particular example of cantilevered plates is perhaps the most thoroughly analyzed configuration, serving as a benchmark example for comparing various modeling approaches (Tosi and Colonious, 2019; Huang, 1995a). The flutter instabilities occurring in these systems can take many forms and critical stability boundaries have been shown to depend on several non-dimensional parameters like the fluid-plate mass ratio M^*, the reduced velocity U^* (inverse Strouhal number) or the Reynolds number Re. Moreover, in cases where the flow is bounded in a channel of a certain height, the confinement ratio H^*(channel height to plate length) is also an important parameter to consider. For example, the works of Shoele and Mittal (2016) or Cisonni et al. (2017) present a large number of benchmark results illustrating the dependence of the linear stability boundaries on several non-dimensional parameters. A classical result in such systems is that of the "cascading" stability boundary in the $(M^* - U^*)$ plane. At low mass ratios, the flutter instability is of the single-mode type, involving the first two *in-vacuo* beam modes. However, as the mass ratio increases, the system develops successive "mode-transitions", whereby the principal flutter instability becomes of the coupled-mode type, involving multiple higher-order beam modes.

In recent years, we have seen an increasing number of studies where the fluid–structure interaction (FSI) system is simulated directly by solving the Navier–Stokes equations in 2D or 3D domains (Cisonni et al., 2017; Tetlow and Lucey, 2009). Such approaches allow for a more realistic representation of the FSI system, as they explicitly account for flow nonlinearities, circulatory flow, viscosity, etc. Yet, the computational cost associated with such approaches becomes a handicap when analyzing systems whose behavior depends on a wide variety of parameters. On this note, 1D models, using simplified equations for the flow, are not only more computationally efficient but also more tractable, and may provide valuable insights into the fundamental physics of the problem. Notably, the discernment of relevant parameters and the interpretation of results become more intuitive.

In the context of simplified approaches, we underline the work of Nagakura and Kaneko (1993) that have used leakage flow theory to model the linear stability of a cantilever beam in a confined narrow passage. More recently, Tosi and Colonious (2019) have compared the stability results from a similar simplified model against those from direct numerical simulations in a 2-D domain. They underline the potential of such modeling approaches as stability boundaries converge over a wide range of non-dimensional parameters, at least for relatively narrow passages.

On the whole, modeling efforts pursued so far deal mostly with the stability analysis, using linearized equations of motions. Knowledge of the conditions for instability and the dependence of various parameters on stability boundaries is undeniably an important aspect of the FSI system dynamics. However, this gives us little insight about the ensuing nonlinear behavior, which might be of valuable interest in various practical applications. For unbounded flows, a number of theoretical and experimental studies can be found, illustrating the variety of possible limit cycles oscillations arising in this type of systems (Taneda, 1968; Tang et al., 2003; Yadykin et al., 2001). In bounded flows, however, modeling presents additional difficulties as the large amplitude motion of the plate will often lead to contact against the channel walls, as various modeling and experimental reports have shown (Wu and Kaneko, 2005; Fujita et al., 2007; Balint and Lucey, 2005).

In a recent work by the authors (Soares et al., 2022), an initial step was taken in the nonlinear analysis of a fluttering cantilever beam in a confined passage. A semi-analytical approach, based on formal solutions for the flow variables, was developed to solve a 1-D model consisting of a cantilever beam surrounded by bounded axial flow on its upper and lower sides. This allowed for the formulation of a closed set of nonlinear ODEs describing coupled FSI dynamics, including flow nonlinearities and flow dissipation through head-loss terms. Additionally, impacts between the flexible beam and the side walls were accounted by including an elastic contact model. Periodic solutions of the FSI system were then pursued through numerical time-domain integrations, revealing a wide variety of limit cycle oscillations, both with and without intermittent impacts, as well as aperiodic dynamics. Henceforth, we will designate this previous formulation as "analytical", as it does not contain any error inducing (spatial-discretization) procedures regarding the flow variables.

The natural next step in the nonlinear analysis of fluttering beams in axial flow is the use of algorithms for the continuation of periodic solutions. Unlike the point-wise description given by time-domain integrations, bifurcation analysis of the system dynamics allows for a wider comprehensive overview of the nonlinear dynamics, as periodic solutions as sought out in a continuous manner with respect to a particular "control" parameter. The harmonic balance method (Krack and Gross, 2019) is a useful and commonly used tool in these contexts, whereby the time-dependent

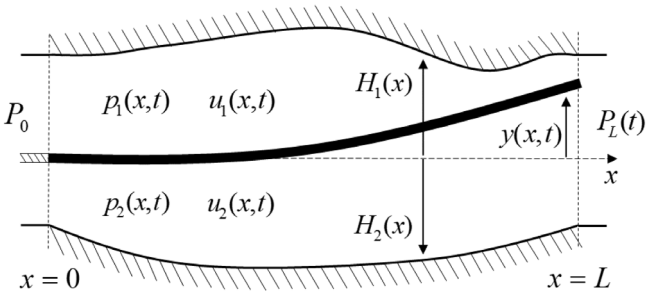

Fig. 1. Diagram of the 1D model.

variables of a nonlinear ODE/DAE system are expanded in a Fourier series, and periodic solutions are then calculated by solving for the Fourier coefficients of the (time) discretized algebraic system. This type of analysis, particularly in the context of simplified formulations, can contribute significantly to the understanding of the underlying physics occurring in these FSI systems and perhaps clarify some persistent and unanswered questions in the field: (1) Is the nature of the Hopf bifurcation in fluttering beams super-critical or sub-critical? (see Eloy et al., 2008; Tang and Paidoussis, 2007); (2) Can the commonly observed hysteretic behavior be explained by multi-stability in certain configurations? ; (3) What is the nature of the aperiodic/chaotic dynamics frequently reported in experiments? In previous work (Soares et al., 2022), an analytical approach was able to decompose the 1-D continuous problem into a set of ODEs. However, an effective time–space separation was not reached as the resulting spatial operators were not constant (i.e. during temporal integrations, for example, the spatial operators need to be calculated at each time-step). Hence, however useful for time-domain integrations of the nonlinear system, this formulation is less adequate for use in continuation algorithms.

In this paper, we seek the establishment of a framework for the bifurcation analysis of these type of FSI systems, by discretizing the continuous problem into a set of time-domain ODE/DAEs (with constant spatial operators). In broad terms, the flow continuity and momentum partial differential equations are converted into sets of time-dependent equations (ODE and algebraic) by expanding the flow velocity and pressure fields in terms of series of space-dependent orthogonal functions, such as Chebyshev or Legendre polynomials. Suitable boundary conditions are obtained by formulating them in terms of the expanded field variables, at the boundary locations. Such procedure follows the so-called Tau-variant of the Galerkin approach, described, for example, in Boyd (2000) and Lanczos (1956). Aside from discretizing the continuous problem into a set of time-dependent differential equations, this approach also provides a formulation with exploitable model reduction capacities, where expansions of the flow velocity, flow pressure or beam motion can be truncated at any suitable number of terms.

In Section 2 the 1-D FSI model is presented and the Galerkin formulation is described in Section 3. Subsequently, in Section 4, several convergence studies are conducted by comparing results from the previously derived theoretical solution (Soares et al., 2022) to those of the present Galerkin formulation, at various orders of truncation for both the flow variables and beam modes, to assess the model reduction capacities of the formulation.

2. Model description

The model presented here deals with the fluid–structure interaction of a flexible beam confined by flow on each upper and lower sides, as illustrated in Fig. 1. Even though the presented formulation is applicable to beams with arbitrary boundary conditions, in this paper we will deal solely with the particular case of cantilevered beams subject to flow from the clamped side to the freely moving side. The flow in each channel is described by bulk-flow equations, where the pressure and velocity fields are taken as cross-sectionally averaged. In the same spirit of formulations based on leakage flow (Inada and Hayama, 1990a), nonlinear localized dissipation at the entrance and exit of the domain is added in the form of head-losses (or pressure losses), which are imposed at the boundary conditions using a classical quasi-static Bernoulli condition.

2.1. Structure dynamics

The dynamics of the beam are defined in a modal framework, i.e. in terms of a finite number (M) of *in-vacuo* beam modes. The dimensionless vertical displacement of the beam $y(x, t)$ is developed as modal summation by

$$y(x,t) = \sum_{m=1}^{M} \phi_m(x) q_m(t) \tag{1}$$

where $q_m(t)$ and $\phi_m(x)$ are the (dimensionless) participation factors and shapes of each beam mode m, respectively. The dynamics of the beam are given, as usual, by the modal equations

$$m_m \ddot{q}_m(t) + 2 m_m \omega_m \zeta_m \dot{q}_m(t) + m_m \omega_m^2 q_m(t) = F_m(t) \quad , \quad m = 1, 2 \ \ldots \ M \tag{2}$$

where m_m, ω_m, ζ_m and $F_m(t)$ are the modal masses, angular frequencies, damping ratios and external forces associated with each beam mode m. Note that all variables are presented in nondimensional form with respect to the characteristic length L, the total mass of the beam $m_0 = \rho_s AL$, and a characteristic frequency $\omega_0 = 2\pi\sqrt{EI/\rho_s A}/L^2$, that is

$$\begin{aligned} x = \underline{x}/L \quad ; \quad t = \underline{t}\omega_0 \\ m_m = \underline{m}_m/m_0 \quad ; \quad \omega_m = \underline{\omega}_m/\omega_0 \quad ; \quad y(x,t) = \underline{y}(x,t)/L \\ q_m(t) = q_m(t)/L \quad ; \quad \dot{q}_m(t) = \dot{\underline{q}}_m(t)/\omega_0 L \quad ; \quad \ddot{q}_m(t) = \ddot{\underline{q}}_m(t)/\omega_0^2 L \end{aligned} \tag{3}$$

where A and EI are the cross-sectional area and bending stiffness of the beam, respectively, and the under-dashes $\underline{x}$ denote the physical variables. The external modal forces $F_m(t)$ are then given by the projection of the flow pressure fields on the upper and lower sides of the beam, $p_1(x,t)$ and $p_2(x,t)$, unto the modal basis, that is

$$F_m(t) = M^* \int_0^1 (p_2(x,t) - p_1(x,t))\phi_m(x)dx \ , \quad m = 1, 2 \ \ldots \ M \tag{4}$$

where the fluid-beam mass ratio is written explicitly as

$$M^* = \frac{\rho L}{\rho_s e} \tag{5}$$

where ρ and ρ_s are the densities of the fluid and the beam, respectively; e denotes the thickness of the beam. The dimensionless pressures are related to the physical pressures by

$$p_c(x,t) = \frac{\underline{p}_c(\underline{x},\underline{t})}{\rho\omega_0^2 L^2} \tag{6}$$

where the subscript c refers to the upper ($c = 1$) or lower ($c = 2$) channels. In Section 2.2, it will become evident that this choice of scaling for the pressure (6) is the most practical, given that the natural normalization for the flow velocities will be $1/\omega_0 L$ and the pressure will be related to flow velocity $p \sim \rho u^2$ (see boundary conditions (12)).

2.2. Fluid dynamics

In the context of bulk-flow theory (Hirs, 1973; Antunes and Piteau, 2010; Piteau and Antunes, 2012), we assume that channel heights are relatively small compared to the characteristic length of the system L. In such scenarios, the variations in the flow pressure $p_c(x,y,z,t)$ and velocity $u_c(x,y,z,t)$ along its cross-section are generally negligible, and hence the flow variables are taken as the cross-sectionally averaged, $p_c(x,t)$ and $u_c(x,t)$. The fluctuating channel heights $h_c(x,t)$ are defined in terms of the channel profiles $H_c(x)$ and the beam motion as

$$\begin{cases} h_1(x,t) = H_1(x) - y(x,t) \\ h_2(x,t) = H_2(x) + y(x,t) \end{cases} \tag{7}$$

where $H_1(x)$ and $H_2(x)$ are the distances from the upper and lower walls to the position of the membrane at rest, respectively. It is worth noting that we assume changes along the channel cross-section $\partial H_c/\partial x$ are sufficiently smooth to avoid flow separation. Then, assuming an inviscid and incompressible flow, the momentum and continuity equations of the fluid for each channel c are given in a nondimensional form by

$$\frac{\partial u_c}{\partial t} + u_c\frac{\partial u_c}{\partial x} + \frac{\partial p_c}{\partial x} = 0 \tag{8}$$

$$\frac{\partial h_c}{\partial t} + \frac{\partial}{\partial x}(h_c u_c) = 0 \tag{9}$$

where the dimensionless channel heights $h_c(x,t)$ are then given explicitly by

$$h_1(x,t) = H_1(x) - \sum_{m=1}^{M}\phi_m(x)q_m(t) \quad ; \quad h_2(x,t) = H_2(x) + \sum_{m=1}^{M}\phi_m(x)q_m(t) \tag{10}$$

where the dimensionless channel profiles are related to the physical profiles by $H_c(x) = \underline{H}_c/L$. The dimensionless flow velocities are related to the physical velocities by

$$u_c(x,t) = \frac{\underline{u}_c(\underline{x},\underline{t})}{\omega_0 L} \tag{11}$$

Note that here, for simplicity, we have neglected distributed head-losses, potentially arising from viscous/boundary effects. Nevertheless, these can easily be incorporated via a distributed dimensionless head-loss frictional term in the form $u_c\,|u_c|f$ or its quadratic simplification $u_c^2 f$, where f is a Fanning friction coefficient, as done for example in Antunes

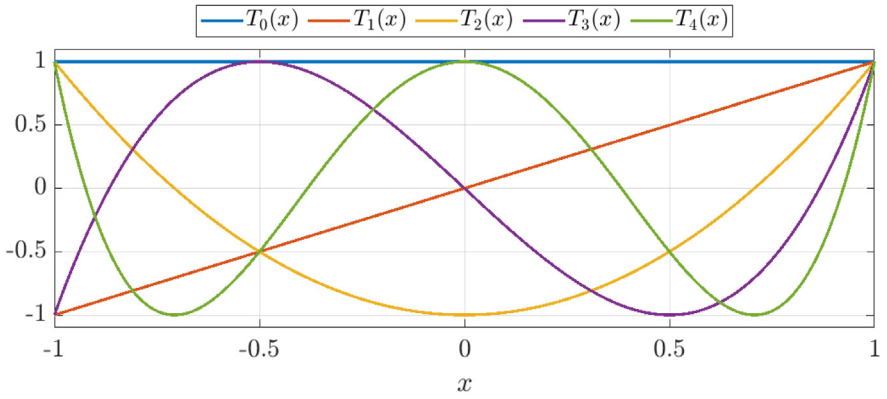

Fig. 2. Chebyshev polynomials of the first kind. (color online).

and Piteau (2010). Nevertheless, flow dissipation is included at the boundaries of the domain. These are enforced at the boundary conditions and aim to encapsulate, in a simplified manner, the energy losses occurring outside the domain. The complex phenomena associated with these energy losses is diverse and can vary significantly with local geometry (e.g. area constriction/expansion) and flow conditions. However, a commonly approach is to use a quasi-steady Bernoulli relation which includes head-loss terms, whose coefficients are typically taken from empirical data. This method is traditionally used to treat leakage-flow instabilities (Nagakura and Kaneko, 1993; Inada and Hayama, 1990a,b). Here, the boundary conditions are set as if two reference pressure chambers (where flow velocity is zero) exist far from the boundaries of the domain. Consequently, the localized head-loss terms will represent energy losses occurring in the path between the reference chambers and the domain entrance/exit. The second order system (8)–(9) is then submitted to the following flow boundary conditions at $x = 0$ and $x = 1$:

$$\begin{aligned} p_c(0,t) &= P_0(t) - \frac{1}{2}\left[u_c(0,t)\right]^2 - \frac{1}{2}\left|u_c(0,t)\right| u_c(0,t) K_0 \\ p_c(1,t) &= P_L(t) - \frac{1}{2}\left[u_c(1,t)\right]^2 + \frac{1}{2}\left|u_c(1,t)\right| u_c(1,t) K_L \end{aligned} \tag{12}$$

where K_0 and K_L are the head-loss coefficients, while P_0 and $P_L(t)$ are the imposed dimensionless pressures at each reference pressure chambers. For configurations with a cantilevered plate/beam, the head-loss coefficient K_0 will not have a significant effect on the dynamics, as it acts on the clamped end of the structure. For steady flow in the positive direction, it acts simply as a control-valve, effectively limiting the flow energy entering the domain. On the other hand, the expected turbulent effects at the trailing-edge suggest that K_L will have a significant effect on the coupling dynamics. For such configurations, several studies have shown that setting $K_0 = 0$ and $K_L = 1$ yields satisfactory results, as predicted stability boundaries compare reasonably well with results from 2-D models (Soares et al., 2022; Tosi and Colonious, 2019) as well as experiments (Nagakura and Kaneko, 1993).

3. Galerkin formulation

Similarly to the expansion procedure done for the beam displacement $y(x,t)$, we assume that both the velocity fields $u_c(x,t)$ and the pressure fields $p_c(x,t)$ are developed in terms of a series of Chebyshev polynomials of the first kind (Fig. 2). These are well suited to, in a compact manner, describe fields with simple linear changes (something that the Fourier series cannot achieve using only a few terms, for example), but also fields of any complexity.

The Chebyshev polynomials of the first kind in the interval $x = [-1, 1]$ are easily computed by the following recurrent relations:

$$T_0(x) = 1 \quad ; \quad T_1(x) = x \quad ; \quad T_n(x) = 2xT_{n-1}(x) - T_{n-2}(x) \tag{13}$$

Similar to the Fourier series, Chebyshev polynomials constitute a complete basis of orthogonal functions. However, note that their orthogonality is not "direct", but with respect to the kernel $w(x) = (1-x^2)^{-1/2}$, that is

$$\int_{-1}^{1} \frac{T_n(x)T_s(x)}{\sqrt{1-x^2}} dx = \begin{cases} \pi & \text{for } n = s = 0 \\ \dfrac{\pi}{2} & \text{for } n = s \neq 0 \\ 0 & \text{for } n \neq s \end{cases} \tag{14}$$

Because we need to project the Chebyshev basis in our domain interval $x = [0, 1]$, we introduce the shifted Chebyshev basis

$$\overline{T}_0(x) = 1 \quad ; \quad \overline{T}_1(x) = 2x - 1 \quad ; \quad \overline{T}_n(x) = 2(2x-1)\overline{T}_{n-1}(x) - \overline{T}_{n-2}(x) \tag{15}$$

and the associated shifted orthogonality kernel

$$\overline{w}(x) = \frac{1}{\sqrt{1-(2x-1)^2}} \tag{16}$$

3.1. Discretization of flow variables

The dimensionless velocity fields at each channel $u_c(x,t)$, truncated to $N+1$ polynomials, are given by

$$u_1(x,t) = \sum_{n=0}^{N} \overline{T}_n(x)\breve{u}_n(t) \quad ; \quad u_2(x,t) = \sum_{n=0}^{N} \overline{T}_n(x)\widehat{u}_n(t) \tag{17}$$

and the dimensionless pressure fields, truncated to $R+1$ polynomials, give

$$p_1(x,t) = \sum_{r=0}^{R} \overline{T}_r(x)\breve{p}_r(t) \quad ; \quad p_2(x,t) = \sum_{r=0}^{R} \overline{T}_r(x)\widehat{p}_r(t) \tag{18}$$

Note that, following standard notation, the first term in the Chebyshev series is taken at $n=0$, i.e. $T_0(x)$. Hence, a sum of polynomials truncated to N (as above) corresponds effectively to a series of $N+1$ polynomials.

Substituting the development for the pressure fields (18) unto the beam equations (2) leads to

$$m_m\ddot{q}_m(t) + 2m_m\omega_m\zeta_m\dot{q}_m(t) + m_m\omega_m^2 q_m(t) = M^* \sum_{r=0}^{R} S_{rm}(\widehat{p}_r(t) - \breve{p}_r(t)) \tag{19}$$

for $m = 1, 2, \ldots, M$, where the spatial operator matrix is given by

$$S_{mr} = \int_0^1 \overline{T}_r(x)\phi_m(x)dx \quad , \quad \begin{cases} r = 0, 1, \ldots, R \\ m = 1, 2, \ldots, M \end{cases} \tag{20}$$

When convenient, to avoid duplication of expression, we will show the discretization procedure of the fluid equations only for the upper channel ($c=1$), even though similar equations will arise for the lower channel ($c=2$). Replacing the developments (17)–(18) into the momentum equation (8), leads to

$$\left(\sum_{n=0}^{N} \overline{T}_n(x)\dot{\breve{u}}_n(t)\right) + \left(\sum_{n=0}^{N} \overline{T}_n(x)\breve{u}_n(t)\right)\left(\sum_{n=0}^{N} \overline{T}_n{}'(x)\breve{u}_n(t)\right) + \left(\sum_{r=0}^{R} \overline{T}_r{}'(x)\breve{p}_r(t)\right) = 0 \tag{21}$$

where the upper dash X' denotes a spatial derivative $\partial/\partial x$. Similarly, replacing the developments (17)–(18) on the continuity equation (9) in the upper channel leads to

$$\begin{aligned} &-\sum_{m=1}^{M} \phi_m(x)\dot{q}_m(t) + H_1'(x)\left(\sum_{n=0}^{N} \overline{T}_n(x)\breve{u}_n(t)\right) + H_1(x)\left(\sum_{n=0}^{N} \overline{T}_n{}'(x)\breve{u}_n(t)\right) \\ &-\left(\sum_{m=1}^{M} \phi_m'(x)q_m(t)\right)\left(\sum_{n=0}^{N} \overline{T}_n(x)\breve{u}_n(t)\right) - \left(\sum_{m=1}^{M} \phi_m(x)q_m(t)\right)\left(\sum_{n=0}^{N} \overline{T}_n{}'(x)\breve{u}_n(t)\right) = 0 \end{aligned} \tag{22}$$

Finally, substituting (17)–(18) into the boundary conditions (12), leads to

$$\sum_{r=0}^{R} \overline{T}_r(0)\breve{p}_r(t) = P_0(t) - \frac{1}{2}\left[\sum_{n=0}^{N} \overline{T}_n(0)\breve{u}_n(t)\right]^2 - \frac{1}{2}\left[\sum_{n=0}^{N} \overline{T}_n(0)\breve{u}_n(t)\right]\left|\sum_{n=0}^{N} \overline{T}_n(0)\breve{u}_n(t)\right| K_0 \tag{23}$$

$$\sum_{r=0}^{R} \overline{T}_r(1)\breve{p}_r(t) = P_L(t) - \frac{1}{2}\left[\sum_{n=0}^{N} \overline{T}_n(1)\breve{u}_n(t)\right]^2 + \frac{1}{2}\left[\sum_{n=0}^{N} \overline{T}_n(1)\breve{u}_n(t)\right]\left|\sum_{n=0}^{N} \overline{T}_n(1)\breve{u}_n(t)\right| K_L \tag{24}$$

3.2. Galerkin projection

Following the typical Galerkin procedure, the momentum and continuity equations (21) and (22) would be projected onto the polynomial series developed for the pressure and for the velocity, respectively. However, if we were to project the continuity equations into the $N+1$ Chebyshev polynomials used to expand the velocity fields and the momentum equations onto the $R+1$ polynomials used for the pressure, we would end up with an overdetermined system, i.e. $2(N+R+2)$ variables and $2(N+R+2)+4$ equations, when the four boundary conditions are taken into account. This issue arises from the fact that, unlike in the case of the beam, for example, the expansion polynomials do not obey the flow boundary conditions.

Hence, we use the so-called "Tau-variant" of the Galerkin method where the projection is made onto a reduced version of the truncated polynomial series (Lanczos, 1956; Boyd, 2000). That is, the continuity equations will be projected unto a reduced basis of only N Chebyshev polynomials and the momentum equations unto R, instead of the usual $N+1$ and $R+1$, respectively. Reducing the projection of each equation by one term, allows the construction of a determined system, including the four boundary conditions. As a note, it is unclear where to truncate the series, i.e. instead of the above mentioned truncation, both continuity equations could be truncated to $N-1$ terms instead, or the momentum equations to $R-1$ terms. All three approaches were attempted and the former was seen to be the most stable numerically.

It will become evident that the orthogonal properties of the Chebyshev polynomials are useful for the projection of the momentum equations as it greatly simplifies the resulting spatial operators. Hence, before the Galerkin projection, we pre-multiply the momentum equations by the (shifted) kernel $\overline{w}(x)$, resulting in the following set of R ordinary differential equations for the upper channel

$$\sum_{n=0}^{N} E_{nr}\dot{\breve{u}}_n(t) + \sum_{n=0}^{N}\sum_{s=0}^{N} F_{nsr}\breve{u}_n(t)\breve{u}_s(t) + \sum_{t=0}^{R} H_{tr}\breve{p}_t(t) = 0 \quad , \quad r = 0, 1, \ldots, R-1 \tag{25}$$

where the associated matrices are given by

$$\begin{aligned}
E_{nr} &= \int_0^1 \overline{T}_n(x)\overline{T}_r(x)\overline{w}(x)dx = \frac{1}{2}\int_{-1}^{1}\frac{T_n(x)T_r(x)}{\sqrt{1-x^2}}dx \quad , \quad \begin{cases} n = 0, 1, \ldots, N \\ r = 0, 1, \ldots, R-1 \end{cases} \\
H_{tr} &= \int_0^1 \overline{T}_t{}'(x)\overline{T}_r(x)\overline{w}(x)dx = \int_{-1}^{1}\frac{T_t{}'(x)T_r(x)}{\sqrt{1-x^2}}dx \quad , \quad \begin{cases} t = 0, 1, \ldots, R \\ r = 0, 1, \ldots, R-1 \end{cases} \\
F_{nsr} &= \int_0^1 \overline{T}_n{}'(x)\overline{T}_s(x)\overline{T}_r(x)\overline{w}(x)dx = \int_{-1}^{1}\frac{T_n{}'(x)T_s(x)T_r(x)}{\sqrt{1-x^2}}dx \quad , \quad \begin{cases} n = 0, 1, \ldots, N \\ s = 0, 1, \ldots, N \\ r = 0, 1, \ldots, R-1 \end{cases}
\end{aligned} \tag{26}$$

Due to the orthogonal properties of the Chebyshev polynomials, the matrices in (26) have relatively simple structures: matrix E_{nr} is diagonal, H_{tr} is sparse upper triangular and the tri-dimensional matrix F_{nsr} also has similar sparsity properties. To clarify, we define these matrices explicitly in the appendix. For the lower channel, an equivalent set of R equations is derived, simply replacing $\breve{u}$ and $\breve{p}$ by $\widehat{u}$ and $\widehat{p}$, in (25).

Contrary to the momentum equations, in the projection of the continuity equations, the usefulness of the orthogonality properties is not clear in a general sense. From (22) one obtains the following sets of N nonlinear algebraic equations, which stand for the continuity equation in the upper and lower channels, respectively,

$$-\sum_{m=1}^{M} A_{mn}r_m(t) + \sum_{s=0}^{N} B_{sn}\breve{u}_s(t) - \sum_{m=1}^{M}\sum_{s=0}^{N} D_{msn}q_m(t)\breve{u}_s(t) = 0 \quad , \quad n = 0, 1, \ldots, N-1 \tag{27}$$

$$\sum_{m=1}^{M} A_{mn}r_m(t) + \sum_{s=0}^{N} C_{sn}\widehat{u}_s(t) + \sum_{m=1}^{M}\sum_{s=0}^{N} D_{msn}q_m(t)\widehat{u}_s(t) = 0 \quad , \quad n = 0, 1, \ldots, N-1 \tag{28}$$

whose dense spatial operators are given explicitly by

$$\begin{aligned}
A_{mn} &= \int_0^1 \phi_m(x)\overline{T}_n(x)dx \quad , \quad \begin{cases} m = 1, 2, \ldots, M \\ n = 0, 1, \ldots, N-1 \end{cases} \\
B_{sn} &= \int_0^1 \left[H_1'(x)\overline{T}_s(x) + H_1(x)\overline{T}_s{}'(x)\right]\overline{T}_n(x)dx \quad , \quad \begin{cases} s = 0, 1, \ldots, N \\ n = 0, 1, \ldots, N-1 \end{cases} \\
C_{sn} &= \int_0^1 \left[H_2'(x)\overline{T}_s(x) + H_2(x)\overline{T}_s{}'(x)\right]\overline{T}_n(x)dx \quad , \quad \begin{cases} s = 0, 1, \ldots, N \\ n = 0, 1, \ldots, N-1 \end{cases} \\
D_{msn} &= \int_0^1 \left[\phi_m'(x)\overline{T}_s(x) + \phi_m(x)\overline{T}_s{}'(x)\right]\overline{T}_n(x)dx \quad , \quad \begin{cases} m = 1, 2, \ldots, M \\ s = 0, 1, \ldots, N \\ n = 0, 1, \ldots, N-1 \end{cases}
\end{aligned} \tag{29}$$

3.3. Formulation of the nonlinear coupled system

The structural modal equations, coupled with the pressure at each channel, can be described as a first-order system by defining the modal velocities $r_m(t) = \dot{q}_m(t)$. In a matrix form, it reads

$$\begin{bmatrix} [\mathbf{I}] & 0 \\ 0 & [\mathbf{I}] \end{bmatrix}\begin{Bmatrix} \{\dot{\mathbf{R}}(t)\} \\ \{\dot{\mathbf{Q}}(t)\} \end{Bmatrix} + \begin{bmatrix} 2[\Omega][Z] & [\Omega]^2 \\ -[\mathbf{I}] & 0 \end{bmatrix}\begin{Bmatrix} \{\mathbf{R}(t)\} \\ \{\mathbf{Q}(t)\} \end{Bmatrix} = \begin{Bmatrix} [\mathbf{M}][\mathbf{S}]\widetilde{\mathbf{P}}(t) - \breve{\mathbf{P}}(t) \\ 0 \end{Bmatrix} \tag{30}$$

where $[\Omega]$ and $[\mathbf{Z}]$ are $M \times M$ diagonal matrices whose diagonals contains the modal frequencies and damping coefficients of the beam, respectively; the $M \times M$ diagonal matrix $[\mathbf{M}]$ is defined by $\mathrm{diag}(\mathbf{M}) = M^*/m_m$; and $\mathbf{R}(t)$, $\mathbf{Q}(t)$, $\breve{\mathbf{P}}(t)$ and $\widehat{\mathbf{P}}(t)$ are column vectors containing the M modal responses of the beam and the $R+1$ pressures at the upper and lower channels, respectively. The matrix $[\mathbf{S}]$ is a $M \times (R+1)$ matrix, whose elements are defined in (20).

Finally, assembling the structural equations (30), the flow continuity equations (27)–(28), the flow momentum equations (25) and the four boundary conditions (23)–(24) leads to the fully coupled nonlinear system,

$$\begin{bmatrix} [\mathbf{I}] & 0 & 0 & 0 & 0 & \cdots & 0 \\ 0 & [\mathbf{I}] & 0 & 0 & 0 & & \\ 0 & 0 & [\mathbf{E}] & 0 & 0 & & \\ 0 & 0 & 0 & [\mathbf{E}] & 0 & & \\ 0 & 0 & 0 & 0 & 0 & & \\ \vdots & & & & & \ddots & \\ 0 & & & & & & 0 \end{bmatrix} \begin{Bmatrix} \dot{\mathbf{R}} \\ \dot{\mathbf{Q}} \\ \dot{\breve{\mathbf{U}}} \\ \dot{\widehat{\mathbf{U}}} \\ \dot{\breve{\mathbf{P}}} \\ \dot{\widehat{\mathbf{P}}} \end{Bmatrix} + \begin{bmatrix} 2[\Omega][Z] & [\Omega]^2 & 0 & 0 & [\mathbf{M}][\mathbf{S}] & -[\mathbf{M}][\mathbf{S}] \\ -[\mathbf{I}] & 0 & 0 & 0 & 0 & 0 \\ 0 & 0 & 0 & 0 & [\mathbf{H}] & 0 \\ 0 & 0 & 0 & 0 & 0 & [\mathbf{H}] \\ -[\mathbf{A}] & 0 & [\mathbf{B}] & 0 & 0 & 0 \\ [\mathbf{A}] & 0 & 0 & [\mathbf{C}] & 0 & 0 \\ 0 & 0 & 0 & 0 & \{\mathbf{T}_0\}^T & 0 \\ 0 & 0 & 0 & 0 & 0 & \{\mathbf{T}_0\}^T \\ 0 & 0 & 0 & 0 & \{\mathbf{T}_L\}^T & 0 \\ 0 & 0 & 0 & 0 & 0 & \{\mathbf{T}_L\}^T \end{bmatrix} \begin{Bmatrix} \mathbf{R} \\ \mathbf{Q} \\ \breve{\mathbf{U}} \\ \widehat{\mathbf{U}} \\ \breve{\mathbf{P}} \\ \widehat{\mathbf{P}} \end{Bmatrix} = \begin{Bmatrix} \mathbf{0} \\ \mathbf{0} \\ -\{\breve{\mathbf{F}}_r\} \\ -\{\widehat{\mathbf{F}}_r\} \\ \{\breve{\mathbf{D}}_n\} \\ -\{\widehat{\mathbf{D}}_n\} \\ \breve{\mathbf{V}}_0 \\ \widehat{\mathbf{V}}_0 \\ \breve{\mathbf{V}}_L \\ \widehat{\mathbf{V}}_L \end{Bmatrix} \tag{31}$$

where the matrices $[\mathbf{A}]$, $[\mathbf{B}]$, $[\mathbf{C}]$, $[\mathbf{E}]$, $[\mathbf{H}]$ and $[\mathbf{S}]$ contain the projection coefficients for the linear terms, defined in (20), (26) and (29). That is:

$$\begin{aligned} &[\mathbf{A}] = A_{nm} \rightarrow \text{size}: N \times M \qquad [\mathbf{E}] = E_{rn} \rightarrow \text{size}: R \times (N+1) \\ &[\mathbf{B}] = B_{ns} \rightarrow \text{size}: N \times (N+1) \quad [\mathbf{H}] = H_{rt} \rightarrow \text{size}: R \times (R+1) \\ &[\mathbf{C}] = C_{ns} \rightarrow \text{size}: N \times (N+1) \quad [\mathbf{S}] = S_{mr} \rightarrow \text{size}: M \times (R+1) \end{aligned} \tag{32}$$

The $R+1$ sized vectors describing the pressure terms on the four flow boundary conditions are given by

$$\begin{aligned} &\{\mathbf{T}_0\} = \overline{T}_r(0) \quad r = 0, 1, 2 \ldots R \\ &\{\mathbf{T}_L\} = \overline{T}_r(1) \quad r = 0, 1, 2 \ldots R \end{aligned} \tag{33}$$

All the nonlinear terms are encapsulated in the right-hand-side of (31). The vectors containing the nonlinear terms in the continuity equations, $\{\breve{\mathbf{D}}_n\}$ and $\{\widehat{\mathbf{D}}_n\}$, and in the momentum equations, $\{\breve{\mathbf{F}}_r\}$ and $\{\widehat{\mathbf{F}}_r\}$, are given by

$$\{\mathbf{D}_n\} = \sum_{m=1}^{M}\sum_{s=0}^{N} D_{msn} q_m(t) u_s(t) \quad ; \quad \{\mathbf{F}_r\} = \sum_{n=0}^{N}\sum_{s=0}^{N} F_{nsr} u_n(t) u_s(t) \tag{34}$$

where the generic $u_s(t)$ is replaced by the velocities in a particular channel, upper $\breve{u}_s(t)$ or lower $\widehat{u}_s(t)$, to obtain the corresponding vectors $\{\breve{\mathbf{D}}_n\}$ and $\{\breve{\mathbf{F}}_r\}$ or $\{\widehat{\mathbf{D}}_n\}$ and $\{\widehat{\mathbf{F}}_r\}$. Finally, the nonlinear terms in the boundary condition equations are given by

$$\begin{aligned} \mathrm{V}_0 &= P_0(t) - \frac{1}{2}\left(1 + \mathrm{sign}\left(\sum_{n=0}^{N} \overline{T}_n(0) u_n(t)\right) K_0\right)\left[\sum_{n=0}^{N} \overline{T}_n(0) u_n(t)\right]^2 \\ \mathrm{V}_\mathrm{L} &= P_L(t) - \frac{1}{2}\left(1 - \mathrm{sign}\left(\sum_{n=0}^{N} \overline{T}_n(1) u_n(t)\right) K_L\right)\left[\sum_{n=0}^{N} \overline{T}_n(1) u_n(t)\right]^2 \end{aligned} \tag{35}$$

where, again, replacing the generic $u_s(t)$ by $\breve{u}_s(t)$ or $\widehat{u}_s(t)$ will yield the corresponding vectors $\{\breve{\mathbf{V}}_0\}$ and $\{\breve{\mathbf{V}}_L\}$ or $\{\widehat{\mathbf{V}}_0\}$ and $\{\widehat{\mathbf{V}}_L\}$.

The coupled system (31) is a system of first-order nonlinear differential–algebraic equations (DAE) of size $2(M+N+R+2)$, the matrix connected with the derivative vector is singular. The state differential variables are $\mathbf{R}$, $\mathbf{Q}$, $\breve{\mathbf{U}}$, $\widehat{\mathbf{U}}$, and the state algebraic variables are $\breve{\mathbf{P}}$, $\widehat{\mathbf{P}}$. Moreover, we note that the DAE system is of differential index-2 (Hairer and Wanner, 1996), as the algebraic equations (flow continuity) do not contain the algebraic variables $\breve{\mathbf{P}}$, $\widehat{\mathbf{P}}$ explicitly. In any case, due to the orthogonality properties of the beam modes $\phi(x)$ and Chebyshev polynomials $T(x)$, the mass matrix will also be diagonal (although singular), which may bring some benefits when calculating solutions numerically.

It is worth mentioning that, the linearized version of this model as already been validated against 2-D viscous models (Tosi and Colonious, 2019; Soares et al., 2022) as well as experiments (Nagakura and Kaneko, 1993). However,

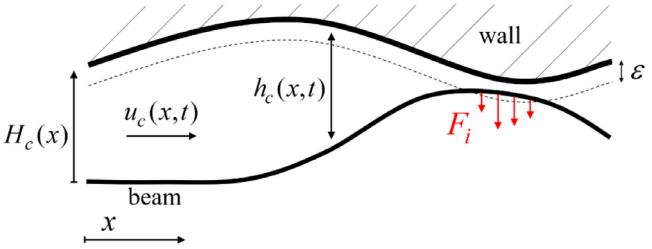

Fig. 3. Illustration of the beam violation right before contact and corresponding impact force. (color online).

rigorous experiments to characterize large amplitude LCOs in this type of systems has not been performed as of yet. Hence, a meaningful experimental validation of the proposed model is not readily available. Nevertheless, the resulting LCOs (more extensive presented in our previous work Soares et al., 2022) seem to be physically plausible, and consistent with experimental observations (Gallegos and Sharmaa, 2019; Lee et al., 2021), at least qualitatively.

3.4. Impact model

Numerous experimental (and modeling) observations (Alben, 2015; Aurégan and Depollier, 1995; Fujita et al., 2007; Lee et al., 2021; Huang, 1995b) demonstrate that nonlinear motions of cantilevered plates in confined axial flow regularly present intermittent impacts between the beam and the side-walls. Consequently, previous attempts at modeling the limit-cycle oscillations (LCO), eventually encountered limitations in their solutions, at regimes where the motion of the plate is large enough that collisions become inevitable.

In the current bulk-flow formulation, the addition of dynamic impact between the beam and the side walls is not a trivial task. One of the major challenges relates to the fact that the solutions for flow velocity and pressure fields present singularities at the moment of contact, i.e. when the channel height $h_c(x,t) = 0$. Consequently, classical penalty methods, reliant on "interpenetration", are incompatible with the flow model, which will result in negative flow gaps. Here, following our previous work (Soares et al., 2022), we use a pragmatic approach to include purely elastic impacts which is compatible with the bulk-flow formulation.

Since the fluid equations do not allow for beam penetration, an impact force $F_i(x,t)$ is applied on the beam before contact, in regions of the beam which have trespassed a small regularization parameter ε (Fig. 3), with $\varepsilon/H \ll 1$. In essence, we allow some flow leakage at the moments of "contact", such that an impact force can applied to the beam without fully restricting the flow dynamics.

Here we use a simplified version of a classic Hertz model where the impact force is linearly proportional to a violation parameter $v(x,t)$, describing the penetration distance between the beam a "virtual" wall defined by $H_c(x)-\varepsilon$, as illustrated in Fig. 9. Then, the impact force $F_i(x,t)$ is given by

$$F_i(x,t) = \begin{cases} k_i\, v_c(x,t) & \text{if } v_c(x,t) > 0 \\ 0 & \text{otherwise} \end{cases} \tag{36}$$

where k_i is an impact stiffness and the violation amplitude is given, in our case, by $v_c(x,t) = \varepsilon - h_c(x,t)$. The sign of $F_i(x,t)$ is defined for each channel: $F_i > 0$ for $c = 2$; $F_i < 0$ for $c = 1$.

Depending on the particular physical problem to be addressed, this modeling approach can surely be refined by including dissipative terms or the flow conditions at the moments of contact. However, this simple pragmatic model is effective enough for the purposes of the current paper. The interested reader can find a more detailed discussion in Soares et al. (2022), where this modeling approach was introduced.

3.5. Linearized system

Often the primary concern in the analysis of FSI systems is related to assessing the conditions leading to linear instability. To linearize the system containing flow nonlinear equations, we firstly separate the governing variables into their steady and fluctuating components. Here, we adopt the conventional notation $g(x,t) = \overline{g}(x) + \tilde{g}(x,t)$. By means of a Taylor-series expansion, we linearize the equations by keeping only the zero-order $\overline{g}(x)$ and first-order $\tilde{g}(x,t)$ components. Because under linearized conditions the flow must assume a particular direction, we use plus-minus $\pm$ and minus-plus $\mp$ signs to distinguish the two cases, and avoid duplication of expressions. The uppers signs are used for flow in the positive direction ($P_0 > P_L$) while the lower signs for flow in the negative direction ($P_0 < P_L$).

For the steady system, we can simply take the original system (31) and remove the time-derivative terms as well as the modal velocities $\mathbf{R}$. Then, the steady system is governed by the following set of $M + 2(N + R + 2)$ nonlinear algebraic

equations

$$\begin{bmatrix} [\Omega]^2 & 0 & 0 & [\mathbf{M}][\mathbf{S}] & -[\mathbf{M}][\mathbf{S}] \\ 0 & 0 & 0 & [\mathbf{H}] & 0 \\ 0 & 0 & 0 & 0 & [\mathbf{H}] \\ 0 & [\mathbf{B}] & 0 & 0 & 0 \\ 0 & 0 & [\mathbf{C}] & 0 & 0 \\ 0 & 0 & 0 & \{\mathbf{T}_0\}^T & 0 \\ 0 & 0 & 0 & 0 & \{\mathbf{T}_0\}^T \\ 0 & 0 & 0 & \{\mathbf{T}_L\}^T & 0 \\ 0 & 0 & 0 & 0 & \{\mathbf{T}_L\}^T \end{bmatrix} \begin{Bmatrix} \overline{\mathbf{Q}} \\ \overline{\breve{\mathbf{U}}} \\ \overline{\widehat{\mathbf{U}}} \\ \overline{\breve{\mathbf{P}}} \\ \overline{\widehat{\mathbf{P}}} \end{Bmatrix} = \begin{Bmatrix} \mathbf{0} \\ -\{\overline{\breve{\mathbf{F}}}_{\mathbf{r}}\} \\ -\{\overline{\widehat{\mathbf{F}}}_{\mathbf{r}}\} \\ \{\overline{\breve{\mathbf{D}}}_{\mathbf{n}}\} \\ -\{\overline{\widehat{\mathbf{D}}}_{\mathbf{n}}\} \\ \overline{\breve{\mathbf{V}}}_0 \\ \overline{\widehat{\mathbf{V}}}_0 \\ \overline{\breve{\mathbf{V}}}_{\mathrm{L}} \\ \overline{\widehat{\mathbf{V}}}_{\mathrm{L}} \end{Bmatrix} \tag{37}$$

The steady components of the nonlinear terms, on the right-hand-side, are given by

$$\{\overline{\mathbf{D}}_n\} = \sum_{m=1}^{M}\sum_{s=0}^{N} D_{msn}\overline{q}_m\overline{u}_s \quad ; \quad \{\overline{\mathbf{F}}_r\} = \sum_{n=0}^{N}\sum_{s=0}^{N} F_{nsr}\overline{u}_n\overline{u}_s \tag{38}$$

$$\begin{aligned} \{\overline{\mathbf{V}}_0\} &= P_0 - \frac{1}{2}(1 \pm K_0)\left[\sum_{n=0}^{N}\overline{T}_n(L)\overline{u}_n\right]^2 \\ \{\overline{\mathbf{V}}_L\} &= P_L - \frac{1}{2}(1 \mp K_L)\left[\sum_{n=0}^{N}\overline{T}_n(L)\overline{u}_n\right]^2 \end{aligned} \tag{39}$$

where the generic $\overline{u}_s$ is replaced by the velocities in a particular channel, upper $\overline{\breve{u}}_s$ or lower $\overline{\widehat{u}}_s$, to obtain the corresponding vectors $\{\overline{\breve{\mathbf{D}}}_n\}$, $\{\overline{\breve{\mathbf{F}}}_r\}$, $\{\overline{\breve{\mathbf{V}}}_0\}$, $\{\overline{\breve{\mathbf{V}}}_L\}$ or $\{\overline{\widehat{\mathbf{D}}}_n\}$, $\{\overline{\widehat{\mathbf{F}}}_r\}$, $\{\overline{\widehat{\mathbf{V}}}_0\}$, $\{\overline{\widehat{\mathbf{V}}}_L\}$.

For the first-order system, we simply linearize the nonlinear terms on the right-hand-side of the original system (31), resulting in

$$\begin{bmatrix} [\mathbf{I}] & 0 & 0 & 0 & 0 & 0 \\ 0 & [\mathbf{I}] & 0 & 0 & 0 & 0 \\ 0 & 0 & [\mathbf{E}] & 0 & 0 & 0 \\ 0 & 0 & 0 & [\mathbf{E}] & 0 & 0 \\ 0 & 0 & 0 & 0 & 0 & 0 \\ 0 & 0 & 0 & 0 & 0 & 0 \\ 0 & 0 & 0 & 0 & 0 & 0 \\ 0 & 0 & 0 & 0 & 0 & 0 \\ 0 & 0 & 0 & 0 & 0 & 0 \end{bmatrix} \begin{Bmatrix} \dot{\mathbf{R}} \\ \dot{\mathbf{Q}} \\ \dot{\breve{\mathbf{U}}} \\ \dot{\widehat{\mathbf{U}}} \\ \dot{\breve{\mathbf{P}}} \\ \dot{\widehat{\mathbf{P}}} \end{Bmatrix} + \begin{bmatrix} 2[\Omega][Z] & [\Omega]^2 & 0 & 0 & [\mathbf{M}][\mathbf{S}] & -[\mathbf{M}][\mathbf{S}] \\ -[\mathbf{I}] & 0 & 0 & 0 & 0 & 0 \\ 0 & 0 & [\tilde{\mathbf{F}}] & 0 & [\mathbf{H}] & 0 \\ 0 & 0 & 0 & [\tilde{\mathbf{F}}] & 0 & [\mathbf{H}] \\ -[\mathbf{A}] & -[\mathbf{D}_2] & [\mathbf{B}]-[\mathbf{D}_1] & 0 & 0 & 0 \\ [\mathbf{A}] & [\mathbf{D}_2] & 0 & [\mathbf{C}]+[\mathbf{D}_1] & 0 & 0 \\ 0 & 0 & \{\tilde{\breve{\mathbf{V}}}_0\} & 0 & \{\mathbf{T}_0\}^T & 0 \\ 0 & 0 & 0 & \{\tilde{\breve{\mathbf{V}}}_0\} & 0 & \{\mathbf{T}_0\}^T \\ 0 & 0 & \{\tilde{\breve{\mathbf{V}}}_L\} & 0 & \{\mathbf{T}_L\}^T & 0 \\ 0 & 0 & 0 & \{\tilde{\breve{\mathbf{V}}}_L\} & 0 & \{\mathbf{T}_L\}^T \end{bmatrix} \begin{Bmatrix} \mathbf{R} \\ \mathbf{Q} \\ \breve{\mathbf{U}} \\ \widehat{\mathbf{U}} \\ \breve{\mathbf{P}} \\ \widehat{\mathbf{P}} \end{Bmatrix} = \{0\} \tag{40}$$

where the linearized components of the nonlinear terms are given by

$$\tilde{\mathbf{F}} = \sum_{n=0}^{N} F_{nsr}\overline{u}_n + \sum_{s=0}^{N} F_{nsr}\overline{u}_s \quad (\text{size } (N+1)\times R) \tag{41}$$

$$\begin{cases} [\mathbf{D}_1] = \displaystyle\sum_{m=1}^{M} D_{msn}\overline{q}_m \quad (\text{size } (N+1)\times N) \\ [\mathbf{D}_2] = \displaystyle\sum_{s=0}^{N} D_{msn}\overline{u}_s \quad (\text{size } M\times N) \end{cases} \tag{42}$$

$$\{\tilde{\mathbf{V}}_0\} = (1 \pm K_0) \sum_{s=0}^{N} \overline{T}_s(0)\overline{T}_n(0)\overline{u}_s \quad \text{(size } 1 \times (N+1)\text{)}$$
$$\{\tilde{\mathbf{V}}_L\} = (1 \mp K_L) \sum_{s=0}^{N} \overline{T}_s(1)\overline{T}_n(1)\overline{u}_s \quad \text{(size } 1 \times (N+1)\text{)} \tag{43}$$

where the generic $\overline{u}_s$ is replaced by the velocities in a particular channel, upper $\overline{u}_s$ or lower $\overline{u}_s$, to obtain the corresponding matrices $\left[\tilde{\mathbf{D}}_2\right]$, $\left[\hat{\mathbf{D}}_2\right]$ and vectors $\{\tilde{\tilde{\mathbf{V}}}_0\}$, $\{\hat{\tilde{\mathbf{V}}}_0\}$, $\{\tilde{\tilde{\mathbf{V}}}_L\}$, $\{\hat{\tilde{\mathbf{V}}}_L\}$.

4. Convergence studies

In this paper we will not present an extensive report of numerical results and will restrict ourselves to showing that the results obtained using this present Galerkin approach are positively validated by those obtained with the analytical solution (Soares et al., 2022). The interested reader is referred to the following works (Tosi and Colonious, 2019; Nagakura and Kaneko, 1993; Soares et al., 2022) where results from the proposed 1-D model have been compared to more realistic 2-D viscous models as well to experiments. Here, we will focus mainly on the convergence properties of the new formulation. Several periodic solutions will be shown using various orders of truncation for our series, both in terms of the Chebyshev polynomials used for the flow variables as well as the mode shapes used for the flexible beam to access the viability for compact formulations in different scenarios.

Following reference studies (Shoele and Mittal, 2016; Cisonni et al., 2017), we will present results in terms of the following dimensionless parameters

$$M^* = \frac{\rho L}{\rho_s e} \quad ; \quad U^* = \frac{U_0}{\omega_0 L} \quad ; \quad H^* = \frac{H_0}{L} \tag{44}$$

where U^* is a reduced velocity (inverse of a Strouhal number), M^* is the fluid-beam mass ratio and H^* is the confinement ratio. In our formulation, $\underline{H}_0 = \underline{H}_1 + \underline{H}_2$ and the fluid velocity U_0 is given by the steady component of the inlet velocity, i.e. $U_0 = (\overline{\overline{u}}_0 + \overline{\overline{u}}_0)/2$.

4.1. Linear stability analysis

In our previous analytical formulation, which did not rely on any error-inducing (discretization) procedures regarding the flow variables, the resulting first-order linearized system was of size $2M + 2$ where the variables were the modal displacements q_m and velocities r_m plus two global unsteady flow rates $\tilde{Q}_c(t)$, one for each channel. The resulting generalized eigenproblem was regular and composed of two dense non-singular matrices. The ensuing $2M+2$ eigenvalues contained $2M$ (coupled) modes associated with the various fluid-loaded beam modes plus two eigenvalues associated with the flow in each channel (trivial steady flow modes, equivalent to flow "rigid body" mode).

However, in the current formulation, the resulting linear DAE system has a singular mass matrix. Such systems are known to produce both finite and infinite eigenvalues. With a few exceptions, infinite eigenvalues are generally attributed to "nondynamic" modes, essentially trivial (for further details, see Soares et al., 2022). Nevertheless, the singular eigenvalue problem can be solved numerically to obtain both finite and infinite eigenvalues (Eigenvalue Solver eig(), 2022). In our linearized DAE system (40), of size $2(M+N+R+2)$, we obtain $2M+2$ finite eigenvalues and $2(N+R)+2$ infinite ones (this is coherent with the results from our analytical formulation). All infinite eigenvalues are associated with purely pressure-based eigenvectors (where all other components of the eigenvectors are null). This is expected since the pressure coefficients $p_r(t)$ are the algebraic variables of the DAE system.

For simplicity, we consider here configurations with flow in the positive direction, i.e. $P_L < P_0$, and symmetric channels with constant height, $H_1 = H_2$. Additionally, we will consider truncations of the Chebyshev terms equal for both the expansions of the velocity and pressure fields, i.e. $N = R$.

As an initial assessment of the current formulation and its model reduction capacities, in Fig. 4, we compare the stability boundaries resulting from the analytical formulation against those from the current approach, using various orders of truncation N for the expansion of the flow variables. The confinement ratio was set at $H^* = 1/10$. In all cases, a relatively large number of beam modes were considered ($M = 20$), to ensure errors associated to the beam discretization were negligible. Modal damping ratios of the beam were fixed for all modes at $\zeta_m = 0.01$.

In Fig. 4(a) we see the typical "cascading" stability boundary discussed in the introduction. The "modal transitions" (occurring at, for example, $M^* \simeq 0.7$ and $M^* \simeq 2.5$) are associated with a change in the shape of the primary unstable (coupled) mode. To illustrate, Fig. 5 shows the neutrally stable (complex) mode shapes $\psi(x)$ at different points (1)–(3) in the cascade of the stability boundary, as indicated in Fig. 4. We notice that at low mass ratios (Fig. 5-(1)) the primary unstable mode shape is composed primarily by components of the 1st and 2nd *in-vacuo* beam modes. However, as the mass ratios increase, the higher order *in-vacuo* beam modes become dominant in the unstable motion. As seen clearly in Fig. 4(b), these transitions in the stability boundary are also accompanied by a discontinuous increase in the instability frequency.

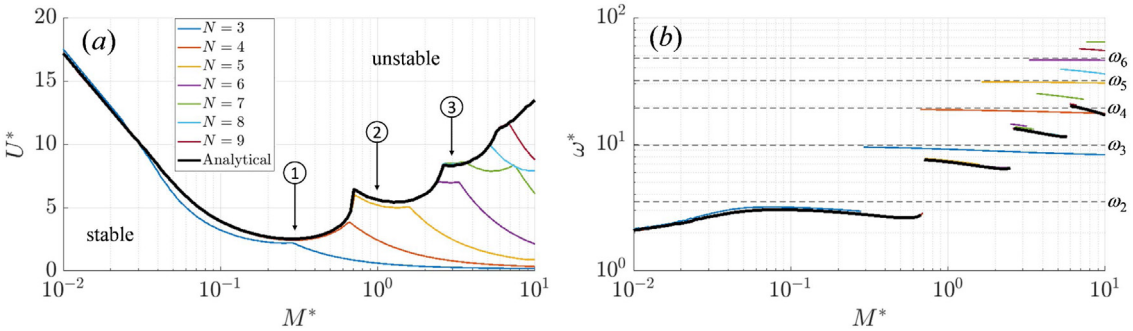

Fig. 4. (a) Stability boundaries in the $(M^* - U^*)$ plane for a system with confinement ratio $H^* = 1/10$, using the analytical formulation (black line) and the Galerkin formulation (colored lines) with various orders of truncation N; (b) Corresponding critical frequencies, where $\omega^* = \omega_{\text{crit}}/\omega_0$. (For interpretation of the references to color in this figure legend, the reader is referred to the web version of this article.)

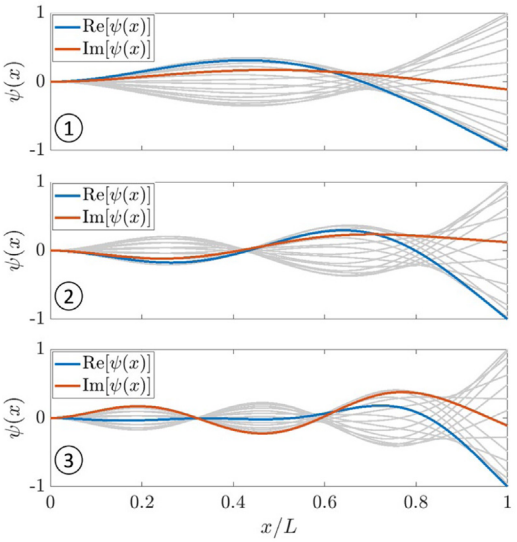

Fig. 5. Complex mode-shapes of the neutrally-stable modes associated with the boundary points (1)–(3), indicated in Fig. 4. The real and imaginary parts of the mode shapes are indicated in blue and red, respectively. The gray lines illustrate the actual beam motion associated with the corresponding complex mode shapes. (For interpretation of the references to color in this figure legend, the reader is referred to the web version of this article.)

With that said, interpretation of the results regarding the convergence of the Galerkin approach becomes more intuitive. In Fig. 4 we note that, for low-to-moderate mass ratios ($M^* \lesssim 1$), a relatively small number of polynomials in the expansion of flow variables ($N > 4$) is sufficient for an accurate description of the stability boundary. However, as mass ratios increase the order of truncation N necessary for converge also increases. Naturally, this is explained by the fact that the spatial distribution of the fluctuations in flow velocity and pressure will accompany the prevailing beam motion. Hence, when higher-order (*in-vacuo*) beam modes are predominant in the unstable motion, the flow velocities and pressures will also require an expansion of Chebyshev polynomials of the same order.

Although not shown here, an investigation regarding the truncation of beam modes M was carried out. As is self-evident, conclusions are similar to those discussed above, i.e. accurate results entail that the considered number of beam modes M include the dominant components of the unstable (fluid–structure coupled) mode. For relatively low mass-ratios ($M^* < 0.5$), as is typically the case for configurations in air, two *in-vacuo* modes ($M = 2$) are generally sufficient. For larger mass-ratios ($M^* > 0.5$), a larger number of beam modes is necessary.

4.2. Nonlinear analysis

We now investigate the viability of the current formulation for solving the fully nonlinear system (including beam-wall impacts) using time-domain integrations. Here, several time-domain solutions will be presented, and compared to results from the analytical formulation, in order to assess the convergence properties of the new formulation in terms of both the truncation of the flow variables expansions $N(= R)$, as well as the number of considered beam modes M.

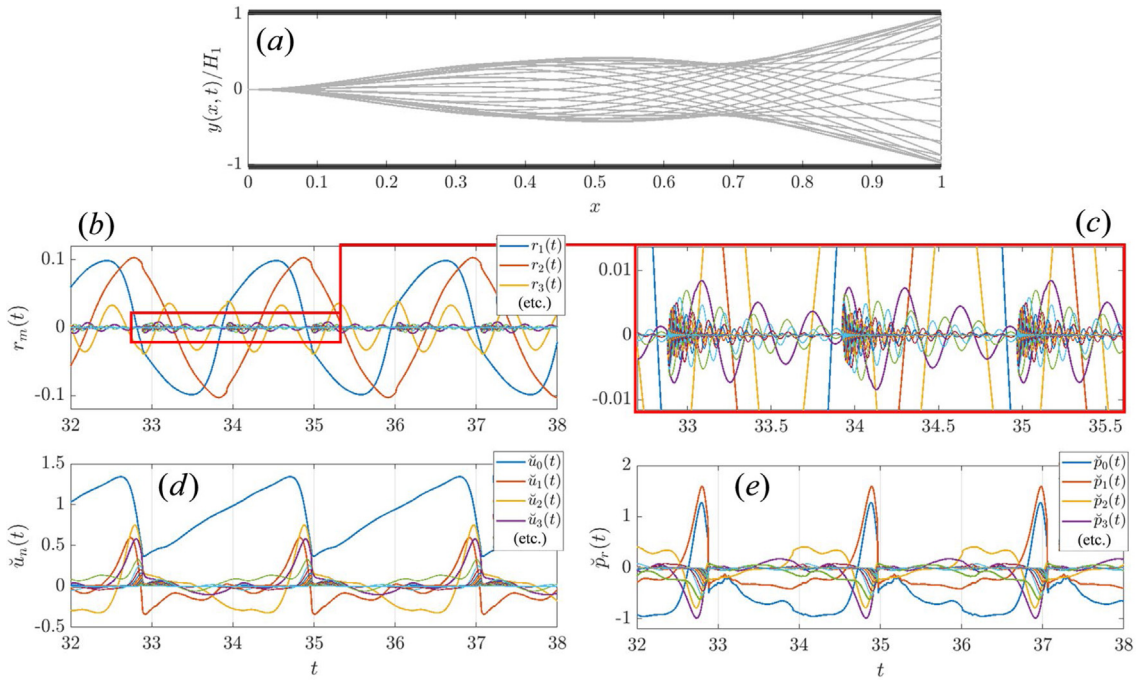

Fig. 6. Overview of the resulting limit-cycle oscillations: (a) snapshots of the beam motion; temporal evolution of the (b) modal velocities; (c) zoom of modal velocities; (d) velocity coefficients and (e) pressure coefficients of the flow in the upper channel. (color online).

The time-domain integrations of the (numerically challenging) DAE system of differential index-2 (31) were performed using an implicit Runge–Kutta scheme based on a 7-stage Radau IIA method. The algorithm can be found on the Matlab's Central File Exchange (Mahooti and Radau, 2020) and was programmed by Meysam Mahooti based on the routine RADAU5 described in Hairer and Wanner (1996).

To illustrate the model reduction capacities of the current approach, we examine an example limit-cycle in a symmetric configuration $H_1 = H_2$, where intermittent impacts occur between the beam-tip and side walls. The main non-dimensional parameters were taken as $H^* = 1/10$, $M^* = 0.1$, $U^* = 8.5$ and $\zeta_m = 0.05$ (for all modes). The value of the dimensionless impact stiffness was set to $k_i = 10^5$, based on the wish to simulate relatively stiff impacts without the having to include an overwhelming amount of beam modes (it will be shown later that $M = 20$ was sufficient to describe impacts accurately). The impact regularization parameter was set to 1% of the channel height, $\varepsilon/\underline{H}_0 = 0.01$, to allow a reasonable margin of contact "penetration".

Firstly, to give an overview of the resulting LCO, Fig. 6 shows (a) snapshots of the beam motion as well as (b) the temporal evolution of the modal velocities $r_m(t)$, (c) the velocity coefficients (d) and pressure coefficients in the upper channel, $\breve{p}_r(t)$ and $\breve{u}_n(t)$ (due to symmetry, the lower channel flow variables are equivalent, but in phase opposition). Here, the truncation of the beam modes and Chebyshev polynomials were set to large values, $M = N = R = 30$, deemed sufficient to describe the LCO accurately, as will be shown in the following sub-sections.

Fig. 6-(b) shows us that the beam motion during the LCO is dominated by the first three *in-vacuo* beam modes. Moreover, we note that higher-order beam modes are excited intermittently after each impact (Fig. 6-(c)). Nevertheless, their influence remains small in the overall LCO pattern. In Fig. 6-(d) and (e), we see that, in general, the most significant oscillations in the flow variables are given by the first 3–4 coefficients of the Chebyshev expansions $\breve{u}_{0-3}(t)$ and $\breve{p}_{0-3}(t)$. This is coherent with what was shown in linear stability analysis, in that the spatial profile of the flow oscillations will typically accompany the motion of the beam. However, right before an impact, many higher-order components $\breve{u}_{n>3}(t)$ and $\breve{p}_{r>3}(t)$ become prominent, meaning that velocity and pressure profiles will present larger (spatial) gradients at these instances.

4.2.1. Convergence of Chebyshev truncation

In this section we aim to assess the model reduction capacities of the present model. Periodic solutions for the configuration presented above (Fig. 6) have been calculated, using various orders of truncations for the velocity and pressure expansions $N(= R)$. Since, in this case, intermittent impacts occur solely at the tip of the beam, and since all *in-vacuo* beam mode shapes $\phi(x)$ contain maxima at the beam-tip, a reasonable global indicator of the LCO is given by the beam-tip velocity $\dot{y}(L,t)$. Fig. 7 shows the phase-portrait of the beam-tip (left) and the temporal evolution of the (normalized) beam-tip velocity $\dot{y}(L,t)$, in solutions calculated with various orders of truncation N. The solution obtained

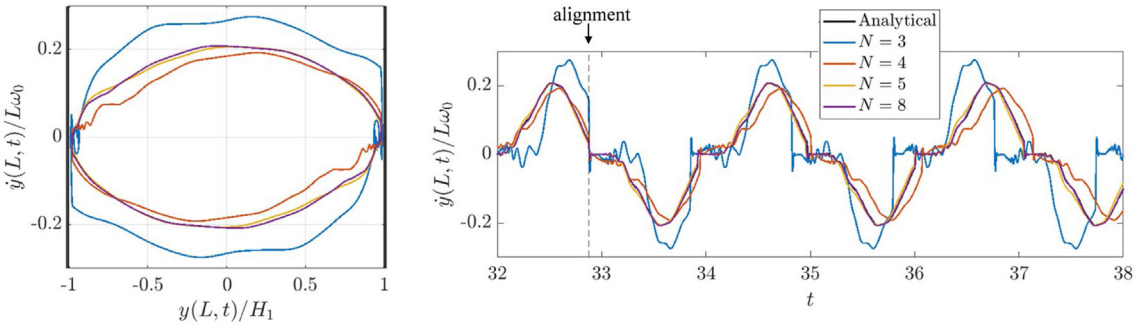

Fig. 7. Phase portrait of the beam-tip during an LCO with intermittent impacts (left) and temporal evolution of the beam-tip velocity $\dot{y}(L,t)$ (right), using various truncations of the Chebyshev expansions $N(=R)$. (color online).

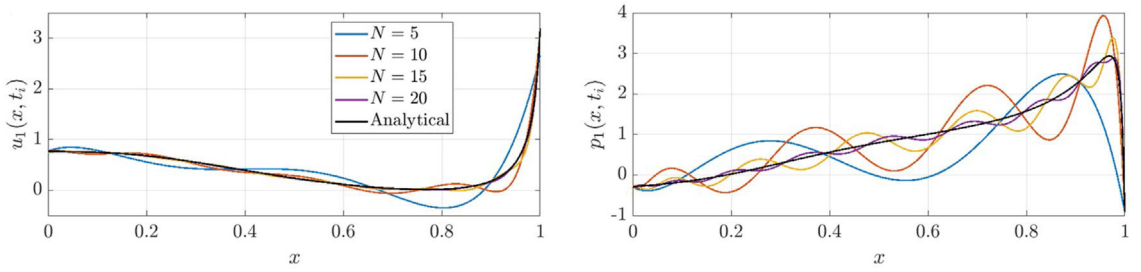

Fig. 8. Description of the velocity (left) and pressure (right) profiles in the upper channel at time t_i, right before contact between the beam-tip and the upper wall, using various truncations for the Chebyshev expansion $N = R$. The corresponding profiles calculated with the analytical model are shown in black. (color online).

with the analytical formulation was also plotted for comparison, even though it is indistinguishable from the solution with $N = 8$ (plots are overlapped). Here, the number of considered beam modes was maintained fixed at $M = 30$.

From Fig. 7 we note that, in fact, the LCO seems to be reasonably well represented by relatively low truncations orders ($N \geq 4$). At truncations above $N \geq 8$, the evolution of the beam-tip velocity (as well as the phase-portrait) is indistinguishable from the analytical results (plots are overlapped). Even at $N = 5$, we notice only very minor quantitative differences. At $N = 4$, deviations start to become more evident, with a noticeable underestimation of the fundamental frequency of oscillation (∼2%). Nevertheless, the overall motion remains relatively well represented. Finally, at $N = 3$ results collapse dramatically, with a gross misrepresentation of the oscillation pattern and a significant overestimation of the fundamental frequency (∼8%).

These observations suggest that, even in the presence of impacts (strong nonlinearities) and the consequent appearance of sharp (spatial) gradients in the profiles of the flow pressure and velocity, the overall LCO can nevertheless be well represented by relatively low truncation orders N. That is, the occurrence of impacts does not seem to have a significant effect on the previously described logic that: the truncation order N must be sufficient to accompany the *dominant* beam motion profile. In this case, the first three *in-vacuo* beam modes dominate, and hence truncations of $N \geq 4$ will in general suffice.

To clarify, Fig. 8 shows the velocity and pressure spatial distribution on the upper channel at a moment t_i before contact between the beam-tip and the upper wall. Here, we notice the very sharp gradients near the beam-tip ($x \approx 1$). As expected, we see that a large order of truncation N is necessary to properly describe the sharp flow gradients, which are severely misrepresented by the solutions using low truncations, showing a very prominent Gibbs effect. However, despite these severe misrepresentations, we have seen that low orders of truncation ($N \geq 4$) are effectively able to reproduce the overall LCO accurately. This could possibly be explained by two reasons: (1) the misrepresentations of the sharp flow profiles are very brief and (2) the observed Gibbs phenomena will be "dissipated" once the (pressure) profiles are projected unto the dominant beam modes (of relatively low-order).

Here it is worth underlining that here we have considered the convergence of the flow fields assuming the same truncation for the pressure and velocity, i.e. $N = R$. In a linear context, where oscillations are arbitrarily small, this is a reasonable assumption as both velocity and pressure fields will tend to have the same gradients (following the beam motion) (Soares et al., 2022). However, in a nonlinear context, flow velocity and pressure profiles can differ significantly, and it is not evident which variable will present larger gradients and hence necessitate larger truncations. Moreover, this also likely a problem-dependent issue. Nevertheless, based on the numerous simulations conducted for this work, our experience suggests that often, the pressure fields will present larger gradients, as illustrated in Fig. 8. This

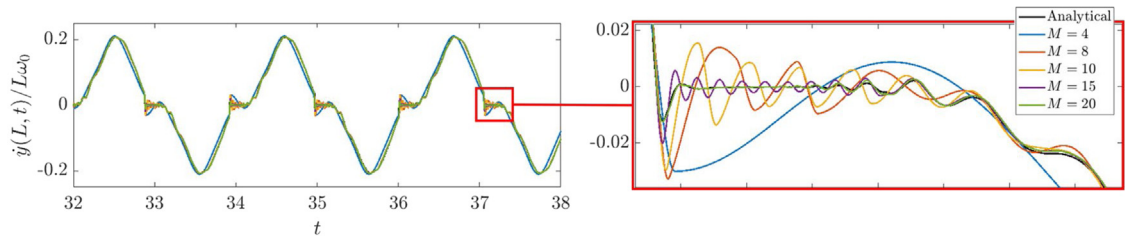

Fig. 9. Temporal evolution of the beam-tip velocity $\dot{y}(L,t)$ during a LCO with intermittent impacts, calculated with different number of considered beam modes M. (color online).

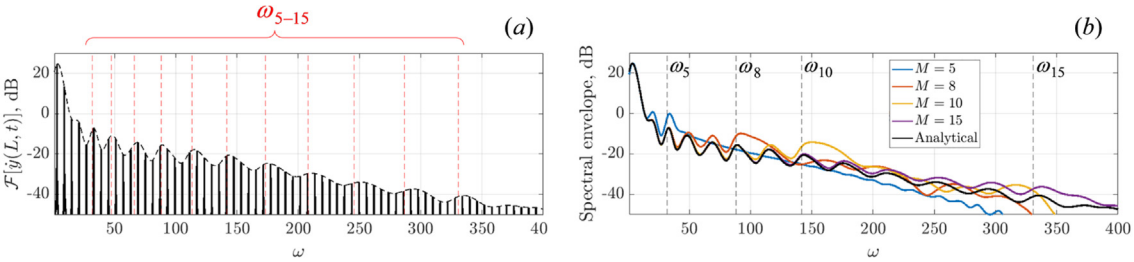

Fig. 10. (a) Spectra of the beam-tip velocity $\dot{y}(L,t)$ in the analytical solution (top); (b) Spectral envelopes of solutions with various beam mode truncations M. (color online).

suggests, tentatively, that using smaller truncations for the velocity field, i.e. $N < R$, could eventually be a viable option. Nevertheless, the studies presented here, with $N = R$ for simplicity, effectively provide a conservative upper bound on the necessary truncation.

4.2.2. Convergence of beam mode truncation

Now we examine that effect of the number of considered modes M on the resulting LCOs. Fig. 9 shows the temporal evolution of the beam-tip velocity in various solutions using a different number of considered beam modes M. Here, the truncation of the Chebyshev expansions used for the flow variables was fixed at $N = R = 30$.

The top plot in Fig. 9 shows us that, in this case, the overall motion of the LCO does not seem to be significantly affected by the number of considered modes M, so long as $M \geq 4$. The main difference between the various solutions is concentrated at the moments of impact (right plot). Impacts generate rapid changes in the velocity of the beam-tip. Consequently, many *in-vacuo* beam modes are excited. We notice that when the number of considered modes is relatively low ($M < 20$), impacts lead to a residual oscillation of the beam-tip. Moreover, is it worth noting that the frequency of these residual oscillations is approximately equal to the frequency of the highest considered mode. This suggests that, at low truncations M, the impact energy transferred to the beam, that would otherwise be distributed evenly between all modes, is going to be concentrated on the highest considered mode (stiffest mode).

To clarify this effect, the spectra (and spectral envelopes) of the beam-tip velocity are shown in Fig. 10. In Fig. 10-(a) we can observe that the motion of the tip is composed of many harmonic components (>100). Moreover, because the beam motion is symmetric, its spectra contain only odd harmonic components. If we perform a (spline) interpolation of the spectral peaks, we can calculate a "spectral envelope", as illustrated in Fig. 10-(a). In this envelope we notice several "formants", whose frequency effectively corresponds to the frequency of the *in-vacuo* beam modes, excited during impacts. In Fig. 10-(b), we notice these formants are modified when a different number of beam modes is considered. More concretely, the energy near the frequency of the highest considered mode M is increased.

Finally, it is worth noting that solutions with $M = 20$ are sufficient to rigorously describe the stiff impacts considered. This is coherent with the general presupposition that the modal stiffness of the highest considered beam mode $m_M\omega_M^2$ must be somewhat larger than the impact stiffness k_i. In this particular case, the dimensionless beam stiffness $m_{20}\omega_{20}^2 = 1.23 \times 10^5$, while the dimensionless impact stiffness $k_i = 10^5$.

5. Conclusion

In this paper we presented a Galerkin formulation for the nonlinear modeling of a flexible beam in confined flow. The motion of a 1-D flexible beam was described in terms of its modes of vibration while the flow velocity and pressure in each channel was spatially discretized via an expansion in terms of a series of space-dependent orthogonal functions, such as Chebyshev polynomials. The tau-variant of the Galerkin approach enabled the enforcement of the nonlinear boundary conditions in a well-posed manner. This led to a purely time-dependent system of nonlinear DAEs of index-2

and presented an elegant framework that can be used for a comprehensive study of the nonlinear dynamics of these FSI systems using bifurcation analysis (e.g. harmonic balance method, continuation, etc.).

Comparisons with previous work (Soares et al., 2022) validated the current approach and allowed us to assess the convergence properties and model reduction capacities of the present formulation, in the context of both linear stability analysis and the calculation of LCOs. The presented convergence studies suggest that, even in the presence of strong nonlinearities stemming from beam-wall impacts, LCOs can be accurately represented using relatively low orders of truncation for the flow variables. In sum, results indicate that the orders of truncation for the expansion of flow variables should be sufficient to accompany the *dominant* beam motion. In realistic scenarios ($M^* < 2$) where contact between the beam and the side-walls do not occur, a truncation of $N \leq 5$ for the flow variables with only two or three beam modes will generally suffice for an accurate description of the LCOs.

Regarding the beam mode truncation, results suggest that even in the presence of stiff impacts, lower orders truncation of beam modes may, at least in some cases, not alter the overall oscillation pattern of the LCO, and still provide fair approximations. This indicates that, despites the presence of intermittent impacts, the fluid–structure interaction continues to play a dominant role in the fluttering dynamics, as similarly reported in a recent experimental study (Lee et al., 2021).

The presented framework can serve as a basis for a comprehensive analysis of the nonlinear dynamics of flexible beams in confined flow. Namely, using bifurcation analysis tools for the calculation and continuation of periodic solutions will contribute to a more comprehensive understanding of the underlying physics occurring in this type of FSI systems. Moreover, the generic methodology presented here can also be adapted to different systems in the field of fluid–structure interaction, providing compact time-dependent formulations for nonlinear analysis.

CRediT authorship contribution statement

Filipe Soares: Methodology, Software, Data curation, Formal analysis, Visualization, Writing – original draft, Writing – review & editing. **Jose Antunes:** Conceptualization, Methodology, Supervision, Writing – review & editing. **Vincent Debut:** Supervision, Writing – review & editing. **Christophe Vergez:** Supervision, Writing – review & editing. **Bruno Cochelin:** Writing – review & editing. **Fabrice Silva:** Writing – review & editing.

Declaration of competing interest

The authors declare that they have no known competing financial interests or personal relationships that could have appeared to influence the work reported in this paper.

Data availability

Data will be made available on request.

Acknowledgment

The authors gratefully acknowledge the financial support given by "Fundação para a Ciência e Tecnologia" (FCT – Portugal) through the PhD grant referenced SFRH/BD/140598/2018.

Appendix. Exploiting the orthogonality of Chebyshev polynomials

Here we illustrate the structure of the matrices (26) resulting from the orthogonal projection of the momentum equations. The matrix associated with the time-derivative of the velocity field is given by

$$E_{nr} = \int_0^1 \overline{T}_n(x)\overline{T}_r(x)\overline{w}(x)dx = \frac{1}{2}\int_{-1}^{1} \frac{T_n(x)T_r(x)}{\sqrt{1-x^2}}dx \quad , \quad \begin{cases} n = 0, 1, \ldots, N \\ r = 0, 1, \ldots, R-1 \end{cases} \tag{45}$$

Notice the relation between the shifted $\overline{T}_n(x)$ and unshifted basis $T_n(x)$. This matrix is diagonal and has the following structure

$$E_{nr} = \frac{\pi}{4}\begin{bmatrix} 2 & 0 & \cdots & 0 \\ 0 & 1 & 0 & \\ \vdots & 0 & 1 & \\ 0 & & & \ddots \end{bmatrix} \tag{46}$$

The matrix associated with the pressure term is

$$H_{tr} = \int_0^1 \overline{T}_t{}'(x)\overline{T}_r(x)\overline{w}(x)dx = \int_{-1}^{1} \frac{T_t{}'(x)T_r(x)}{\sqrt{1-x^2}}dx \quad , \quad \begin{cases} t = 0, 1, \ldots, R \\ r = 0, 1, \ldots, R-1 \end{cases} \tag{47}$$

and has the following upper-triangular structure

$$H_{tr} = \pi \begin{bmatrix} 0 & 1 & 0 & 3 & 0 & 5 & 0 & \\ & 0 & 2 & 0 & 4 & \ddots & 6 & \\ & & 0 & 3 & \ddots & 5 & 0 & \ddots \\ \vdots & & & \ddots & 4 & 0 & 6 & \\ & & & & 0 & 5 & 0 & \ddots \\ & & & & & 0 & 6 & \\ 0 & & & & & & \ddots & \end{bmatrix} \tag{48}$$

The tri-dimensional matrix associated with the nonlinear convection term is given by

$$F_{nsr} = \int_0^L \overline{T}_n{}'(x)\overline{T}_s(x)\overline{T}_r(x)w(x)dx = \int_{-1}^{1} \frac{T_n'(x)T_s(x)T_r(x)}{\sqrt{1-x^2}}dx \quad , \quad \begin{cases} n = 0, 1, \ldots, N \\ s = 0, 1, \ldots, N \\ r = 0, 1, \ldots, R-1 \end{cases} \tag{49}$$

and its structure can be illustrated by the following

$$F_{0sr} = 0 \; ; \quad F_{1sr} = \frac{\pi}{2} \begin{bmatrix} 2 & 0 & 0 & \cdots & 0 \\ 0 & 1 & 0 & & \\ 0 & 0 & 1 & & \\ \vdots & & & \ddots & \\ 0 & & & & \end{bmatrix} \; ; \quad F_{2sr} = \pi \begin{bmatrix} 0 & 2 & 0 & \cdots & 0 \\ 2 & 0 & 1 & \ddots & \\ 0 & 1 & 0 & 1 & 0 \\ \vdots & \ddots & 1 & & \ddots \\ 0 & & 0 & \ddots & \end{bmatrix}$$

$$F_{3sr} = \frac{3\pi}{2} \begin{bmatrix} 2 & 0 & 2 & 0 & \cdots & 0 \\ 0 & 2 & 0 & 1 & 0 & \\ 2 & 0 & 1 & 0 & 1 & \\ 0 & 1 & 0 & 1 & \ddots & \ddots \\ \vdots & 0 & 1 & \ddots & \ddots & \\ 0 & & & \ddots & & \end{bmatrix} \; ; \quad F_{4sr} = 2\pi \begin{bmatrix} 0 & 2 & 0 & 2 & 0 & 0 & \cdots & 0 \\ 2 & 0 & 2 & 0 & 1 & 0 & & \\ 0 & 2 & 0 & 1 & 0 & 1 & \ddots & \\ 2 & 0 & 1 & \ddots & 1 & \ddots & \ddots & \\ 0 & 1 & 0 & 1 & & \ddots & & \\ 0 & 0 & 1 & \ddots & \ddots & & & \\ \vdots & & \ddots & \ddots & & & & \\ 0 & & & & & & & \end{bmatrix} \; ; \quad \text{etc.} \tag{50}$$

References

Alben, S., 2015. Flag flutter in inviscid channel flow. Phys. Fluids 27.

Antunes, J., Piteau, P., 2010. A nonlinear analytical model for the squeeze-film dynamics of parallel plates subject to axial flow. J. Fluids Struct. 52, 1491–1504.

Aurégan, Y., Depollier, C., 1995. Snoring: Linear stability analysis and in-vitro experiments. J. Sound Vib. 188 (1), 39–54.

Avanzini, F., Walstijn, M., 2004. Modelling the mechanical response of the reed-mouthpiece-lip system of a clarinet. Part 1: a one-dimensional distributed model. Acta Acust. United Acust. 90, 537–547.

Balint, T., Lucey, A., 2005. Instability of a cantilevered flexible plate in viscous channel flow. J. Fluids Struct. 20, 893–912.

Boyd, J.P., 2000. The tau-method. In: Chebyshev and Fourier Spectral Methods. Dover Publications, New York, USA, pp. 473–479.

Cisonni, J., Lucey, A., Elliot, N., Heil, M., 2017. The stability of a flexible cantilever in viscous channel flow. J. Sound Vib..

Eigenvalue Solver eig(), 2022. Mathworks. [Online]. Available: https://www.mathworks.com/help/matlab/ref/eig.html [Accessed in 2022].

Eloy, C., Lagrange, R., Souilliez, C., Schouveiler, L., 2008. Aeroelastic instability of cantilevered flexible plates in uniform flow. J. Fluid Mech. 611, 97–106.

Fujita, K., Morikazu, H., Shintani, A., 2007. A consideration on pre- and post-instability of an axisymmetric elastic beam subject to axil leakage flow. J. Fluids Struct. 23, 463–478.

Gallegos, R., Sharmaa, R., 2019. Small flags in rectangular channels: Dynamics and mean wake characteristics. Int. J. Mech. Sci. 155, 518–535.

Guo, C., Paidoussis, M., 2000. Stability of rectangular plates with free-edges in two-dimensional inviscid channel flow. J. Appl. Mech. 67, 171–176.

Hairer, E., Wanner, G., 1996. Solving Ordinary Differential Equations II: Stiff and Differential-Algebraic Problems. Springer-Verlag, New York.

Hidalgo, P., Jha, S., Glezer, A., 2015. Enhanced heat transfer in air cooled heat sinks using aeroelastically fluttering reeds. In: Thermal Investigations of ICs and Systems. THERMINIC, pp. 1–6.

Hirs, G., 1973. A bulk-flow theory for turbulence in lubricant films. ASME J. Lubr. Technol. 95, 137–146.

Huang, L., 1995a. Flutter of cantilevered plates in axial flow. J. Fluids Struct. 9, 127–147.

Huang, L., 1995b. Mechanical modeling of palatal snoring. J. Acoust. Soc. Am. 97, 3642–3648.
Inada, F., Hayama, S., 1990a. A study on the leakage-flow-induced vibrations. Part 1: Fluid dynamic forces and moments acting on the walls of a narrow tapered passage. J. Fluids Struct. 4, 395–412.
Inada, F., Hayama, S., 1990b. A study on the leakage-flow-induced vibrations. Part 2: Stability analysis and experiments for two-degree-of-freedom systems combining translational and rotational motions. J. Fluids Struct. 4, 413–428.
Krack, M., Gross, J., 2019. Harmonic Balance for Nonlinear Vibration Problems. Springer.
Lanczos, C., 1956. The tau-method. In: Applied Analysis. Prentice Hall, Englewood Cliffs, USA, pp. 465–469.
Lee, J., Kim, D., Kim, H.-Y., 2021. Contact behavior of a fluttering flag with an adjacent plate. Phys. Fluids 33.
Mahooti, M., Radau, II, A., 2020. MATLAB central file exchange. [Online]. Available: https://www.mathworks.com/matlabcentral/fileexchange/56162-radau-iia.
Nagakura, H., Kaneko, S., 1993. Stability of a cantiliver beam subject to one-dimensional leakage flow. In: Proceedings Asia-Pacific Conference '93, Kitakyushiu, Japan, Vol. 1. pp. 352–359.
Nagakura, T., Kaneko, S., Inada, F., Kato, M., Ishihara, K., Nishihara, T., Mureithi, N., 2014. Flow-Induced Vibrations: Classifications and Lessons from Practical Experiences. Academic Press, San Diego, California.
Paidoussis, M.P., 2004. Fluid-Structure Interactions: Slender Structures and Axial Flow. Academic Press, San Diego, California.
Piteau, P., Antunes, J., 2012. A theoretical model and experiments on the nonlinear dynamics of parallel plates subject to laminar/turbulent squeeze-film forces. J. Fluids Struct. 33, 1–18.
Shoele, K., Mittal, R., 2016. Flutter instability of a thin flexible plate in a channel. J. Fluid Mech. 786, 29–46.
Soares, F., Antunes, J., Debut, V., Christophe Vergez, B.C., Silva, F., 2022. A nonlinear analytical formulation for the 1D modelling of a flexible beam in channel flow. J. Fluids Struct. 113.
Taneda, S., 1968. Waving motions of flags. J. Phys. Soc. Japan 24 (2), 392–401.
Tang, L., Paidoussis, M., 2007. On the instability and post-critical behaviour of two-dimensional cantilevered flexible plates in axial flow. J. Sound Vib. 305, 97–115.
Tang, D., Yamamoto, H., Dowell, E., 2003. Flutter and limit cycle oscillations of two-dimensional panels in three-dimensional axial flow. J. Fluids Struct. 17, 225–242.
Tetlow, G., Lucey, A., 2009. Motions of a cantilevered flexible plate in viscous channel flow driven by a constant pressure drop. Commun. Numer. Methods. Eng..
Tosi, L.P., Colonious, T., 2019. Modelling and simulation of a fluttering cantilever in channel flow. J. Fluids Struct..
Wu, X., Kaneko, S., 2005. Linear and nonlinear analyses of sheet flutter induced by leakage flow. J. Fluids Struct. 20, 927–948.
Yadykin, Y., Tenetov, V., Levin, D., 2001. The flow induced vibration of a flexible strip hanging vertically in parallel flow. Part 1: temporal aeroelastic instability. J. Fluids Struct. 15, 1167–1185.